Microstructure in non-standard heavy section ductile iron castings: influence of solidification time and casting size

Article

Microstructure in non-standard heavy section ductile iron castings: influence of solidification time and casting size

Gianluca Di Egidio[1], Paolo Ferro[2], Alessandro Morri[1]

[1] Department of Industrial Engineering (DIN), Alma Mater Studiorum - University of Bologna, Viale del Risorgimento 4, Bologna 40136, Italy

[2] Department of Management and Engineering, University of Padova, Stradella S. Nicola 2, Vicenza I-36100, Italy

gianluca.diegidio2@unibo.it, paolo.ferro@unipd.it, alessandro.morri4@unibo.it,

* Corresponding author: Gianluca Di Egidio; E-mail address: gianluca.diegidio2@unibo.it

Abstract

Ductile iron (DI) represents an optimal solution for saving material and costs in producing large heavy-section castings in the energy sector. It aimed to investigate the influence of very long solidification time (3, 10 and 20 h) in different casting zones (casting center and transition zone) on the microstructure and mechanical properties of non-standard heavy-section ferritic DI (EN-GJS-400-15) castings. The different solidification conditions significantly influenced the microstructure (graphite and ferrous matrix). The extent of phenomena such as degenerate graphite, solidification defects, hard carbides, and intergranular pearlitic areas, and the microstructural coarsening were proportional to the solidification time and attributable to the combined effect of limited undercooling, solid solution diffusion mechanisms, and segregation phenomena. For comparable solidification time, the transition zone was characterized by larger nodules, comparable nodularity, and lower nodule count than the casting center due to more effective diffusion phenomena during cooling. Moreover, the lower segregation phenomena in the transition zone reduced the amount of perlite and carbides in the intercellular zones. Hardness was only slightly influenced by the different solidification conditions and did not represent a reliable indicator of the microstructural inhomogeneities. These results are essential to refine casting simulations for producing large ferritic DI castings, considering the wide microstructural variability within non-standard heavy-section castings caused by significantly different solidification conditions.

Keywords: Heavy-section casting; Ferritic ductile iron; Microstructure; Solidification defects; Graphite degeneration; Hardness

1 Introduction

Today, industrial design and production are oriented towards reducing the environmental impact of mechanical components and require materials suitable for this purpose. Ductile irons (DI), known as nodular irons or spheroidal

graphite irons, offer sustainable and cost-effective solutions for various industrial sectors, such as automotive, heavy industry, and energy. The low pouring temperature and high recyclability reduce the consumption of energy and raw materials and, consequently, the environmental impact of their industrial production [1–2]. Furthermore, excellent castability, good mechanical properties (high tensile strength, good wear resistance, and ductility), and lower cost compared to steels with comparable mechanical properties make DI an effective alternative for producing large structural parts with complex geometry, such as railway brake discs, drive shafts, heavy-duty wheels, and gears, without using joints or welding [3, 4]. For these reasons, DI have experienced continuous global growth since 1965 (the only case with aluminum alloys among casting materials), which is expected to continue, considering the growing use of DI for producing wind turbine components and nuclear storage barrels, encouraged by the ever-increasing demand for renewable energy sources [5].

DI have a composite-like microstructure constituted by graphite nodules dispersed in a ferrous matrix (ferritic or pearlitic), depending on chemical composition, casting conditions, and heat treatment. The long solidification times of heavy-section ductile iron (HSDI) castings generally promote the formation of a ferritic matrix due to a depletion of carbon in the matrix in favor of the growth of graphite nodules [6, 7]. The complex solidification conditions that occur in HSDI castings induce strong microstructural variability and have a negative impact on the mechanical properties (strength, ductility, fatigue resistance, and impact resistance) of the alloy, making the design of large structural components difficult [8]. In particular, long solidification times increase the risk of forming defects such as non-metallic inclusions, shrinkage voids, undesired segregation phenomena of low-melting elements and carbide precipitation at grain boundaries, or degenerated graphite, such as chunky graphite, spiky graphite, exploded graphite, and compacted graphite [9–11]. The HSDI castings present a high sensitivity to tramp elements deriving from recycled steel scrap used as filler materials for DI melting since the long solidification times favor the local segregation of these elements at the grain boundaries, thus worsening the mechanical behavior of the alloy [4, 12]. This is significant because the content of undesirable elements in steel scrap, such as Cr, Mn, Mo, Nb, and V, is expected to increase in the coming years due to the growing content of alloying elements in steels to obtain higher mechanical properties [12–14].

Over the last five years, several studies were conducted to identify possible solutions (modification of the chemical composition, identification of possible correlations between solidification time, microstructure and mechanical properties, optimization of heat treatments) to counteract the decrease in mechanical performance due to the complex solidification conditions in ferritic HSDI castings, given the growing interest in their use in the ecological transition. Feng et al. [15] highlighted the positive effect of Bi in eliminating coarse graphite caused by the degeneration of the excessive spheroidizing inoculation in HSDI, while Yamamoto et al. [16] showed the beneficial effect of Fe–Si–Ca–Zr and Fe–Si–Ca–Ba post-inoculants in increasing the nodule count and impact toughness of ferritic HSDI. Sertucha et al. [17] showed the positive effects of the combined use of Sn, Sb, and rare earths (RE) to decrease chunky graphite appearance, reducing its negative impact on the room temperature mechanical properties of small castings, with a controlled solidification procedure to simulate the solidification conditions in the HSDI castings.

Borsato et al. [9] showed the combined effect of poor inoculation treatment and long solidification time (3 h) on the mechanical properties of the EN GJS 700-2, which led to a decrease in static and cyclic mechanical properties due to a significant increase in grain size, graphite degeneration, segregation of alloying elements and shrinkage voids. Similarly, Benedetti et al. [1] reported an increase in microstructural anomalies (shrinkage voids and graphite degeneration) in the EN-GJS-400-15 by increasing the solidification time (from 2 h 45 min to 12 h) and a consequent decrease in the ultimate tensile strength, elongation to failure and rotating bending fatigue strength by 27.2%, 73.6%, and 30.7%, respectively. A comparable trend was reported by Borsato et al. [10] for a solution-strengthened ferritic DI: the fatigue strength was reduced by 33% when the solidification time was increased from 10 min to 10 h due to an increase in the number and size of defects, such as graphite degeneration and shrinkage porosities, which acted as crack initiation sites.

Other studies emphasized the effects of heat treatments on HSDI castings. Tong et al. [18] evaluated the effects of a series of quenching-tempering treatments on ferritic ductile iron poured into a sand mold of wall thickness > 110 mm, showing the best mechanical properties after austenizing at 880 °C, quenching, and tempering at 570 °C due to the formation of granular pearlite in the matrix. Gundlach et al. [19] demonstrated the efficiency of the air-cooling from an intercritical (IC) temperature in increasing the strength and ductility of ductile iron in sections up to 250 mm, owing to the formation of an acicular pearlite in ferrite structure.

However, the latest studies on HSDI castings were conducted on small batches of laboratory castings that reproduce long solidification times or samples extracted from Y-blocks, which are hardly capable of reproducing the real production conditions of very large HSDI castings. As reported by several authors [20–22], significant differences in graphite nodule and ferrous matrix characteristics were found when experimental samples were extracted from different zones of large castings compared to samples produced under controlled experimental solidification conditions. The microstructure and mechanical properties of non-standard-sized HSDI castings can, in fact, significantly deviate from data obtained from small castings under near-ideal controlled solidification conditions obtained in the laboratory, which are only able to partially reproduce the heterogeneous microstructure and typical defects found in large real components. Furthermore, no data about HSDI castings characterized by sections greater than 200 mm are currently reported in the EN 1563:18 standard, representing a further limitation for their design and use. This is where the need arises to obtain empirical data by directly studying the influence of different solidification conditions in different areas of out-of-standard HSDI castings, thus enabling the development of more accurate predictive solidification and mechanical behavior models [11, 23]. In this scenario, this work aims to provide a starting point for the redefinition of the design rules of HSDI castings characterized by wall thickness larger than 350 mm, currently absent in the literature, providing experimental data and valuable solidification time-microstructure-defect correlations to develop future predictive models. In particular, the effect of very long solidification times was directly evaluated on air-cooled heavy-section castings, thus differing from previous studies [3, 6, 7, 9]. Ferritic DI castings (nominally, EN-GJS-400-15 according to EN 1563:18) were produced in the form of cubes with sides in the range between 350 and 1000 mm to reproduce different solidification times (from 3 to 20 h) in different casting zones (casting center and transition zone). Five Italian foundries were involved in the research project to obtain representative results. This led to the production of castings being independent from a specific foundry practice, strengthening the validity of the experimental data and differentiating

this work from what is currently reported in the literature [3, 6, 7, 9–11, 23], where the data were obtained from experimental material provided by individual founders. In-depth microstructural characterization was performed using optical and electron microscopy for an accurate microstructure-solidification time correlation. Finally, hardness tests were carried out to assess the influence of long solidification times on the mechanical properties of the alloy.

2 Experimental

2.1 Casting production

Five different foundries were involved in casting large-sided cubes: (i) 350 mm^3, (ii) 700 mm^3, and (iii) 1000 mm^3. The cube sizes were assessed by a preliminary numerical simulation according to target solidification times (3, 10 and 20 h) at the casting center, with a tolerance of ± 10%. For the sake of simplicity, the mold was considered to have already been filled with liquid iron at a starting temperature of 1340 °C, therefore avoiding the simulation of any casting system. Around the mold cavity, a sand thickness of 300 mm at an initial temperature of 20 °C was considered (as in real conditions). The whole system (sand mold and iron casting) was modeled with finite elements modeling (FEM). The FEM analysis divided the solid into 10 mm cubes, thus evaluating the centers of adjacent cubes as single points and calculating their interaction via heat transfer equations. As in real conditions, no coolers were considered. The cast iron and sand properties as a function of temperature were taken from the database of the numerical code (Magmasoft©) used to make the casting model: the properties of the cast iron with C = 3.5 wt.% and Si = 2.5 wt.% were chosen. Finally, the heat transfer coefficient (HTC) value between the sand and the alloy as a function of temperature is given in Table 1. The values of this critical parameter are the result of the calibration procedure and experience carried out over several years by the foundries that performed the simulations for this work.

Table 1 Heat transfer coefficient (HTC) as a function of temperature used in simulation

T/°C	20	600	1100	1200	2000
HTC/(W m^{-2} K^{-1})	300	500	600	800	800

Material removal operations were performed to analyze the solidification conditions from blanks obtained by the different zones of the cubes according to the casting simulation (Fig. 1). For each cube, the blanks were extracted by saw cutting, without thermally altering the metallurgical state of the cast iron, and according to the cutting scheme in Fig. 1b, to obtain samples representative of the solidification conditions reported in Table 2. The position of the blanks was based on the solidification simulations within the tolerances mentioned above. The sectioning resulted in the creation of 30 mm × 30 mm × 300 mm blanks from which the samples for the microstructural analyses were obtained.

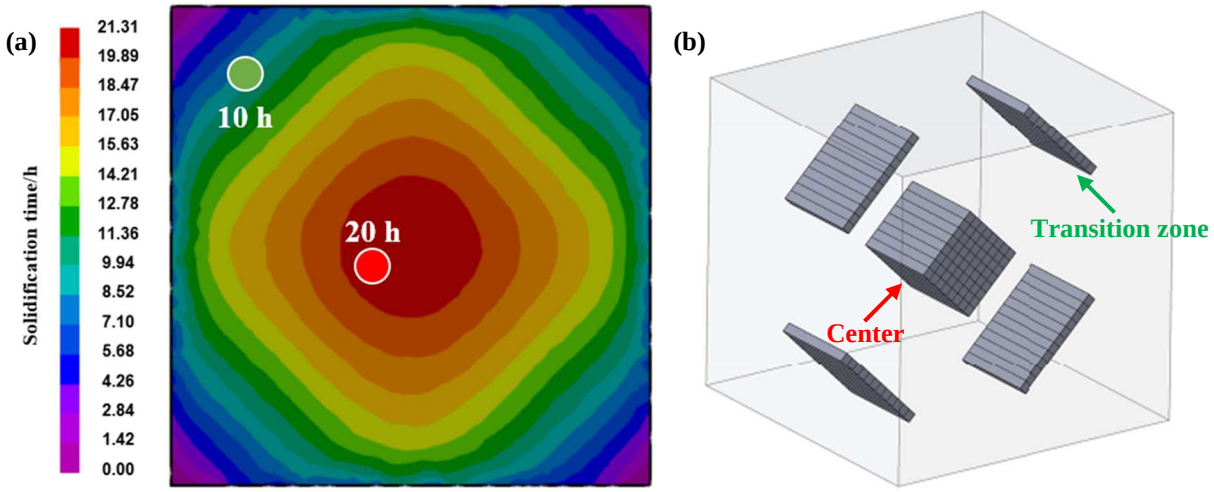

Fig. 1 Casting simulation of 1000 mm × 1000 mm × 1000 mm cube (**a**) and extraction zones (center and transition zone) of specimens from 1000 mm^3 cube (**b**)

Table 2 Designation of analyzed conditions. Blanks are extracted from different areas of cubes to evaluate influence of solidification time and position on microstructure and mechanical properties of EN-GJS-400-15

Designation	Cube	Extraction zone	Solidification time
3C	350 mm × 350 mm × 350 mm	Center	3 h
10C	700 mm × 700 mm × 700 mm	Center	10 h
10T	1000 mm × 1000 mm × 1000 mm	Transition zone	10 h
20C	1000 mm × 1000 mm × 1000 mm	Center	20 h

The study of different solidification times at the center of massive castings aimed to evaluate their effects on the microstructure and defects. Additionally, as highlighted in Fig. 1 and Table 2, also blanks extracted from the transition zone of 1000 mm × 1000 mm × 1000 mm cubes (with a solidification time of 10 h) were studied to compare the solidified microstructures at the center of the cubes with those of areas characterized by comparable solidification times but different solidification conditions (transition zones).

The DI used for the castings was the ferritic EN-GJS-400-15 (according to EN 1563:18). Each foundry melted and poured a standard chemical composition (Table 3), using a comparable casting temperature (1340 °C), and an appropriate casting system. To avoid graphite degeneration, Sb was introduced in the following concentrations: 25 ± 5 × 10^{-6} for the 350 mm side castings and 50 ± 10 × 10^{-6} for the remaining castings, while inoculation and spheroidization treatments were left to the experience of each foundry. After solidification of the castings, the chemical composition of each cube was verified by each foundry using optical emission spectroscopy (Table 3) to assess its compliance with the EN 1563:18 standard.

Table 3 Nominal chemical composition (wt.%) of EN-GJS-400-15 according to EN 1563:18 and average chemical composition of each cube (size 350, 700 and1000 mm^3), evaluated by optical emission spectroscopy

C	Si	Mn	Cu	Ni	Cr	Mo	Sn	V	Ti	S	P	Mg

Min	3.5	2.2	0.1	-	-	-	-	-	-	-	-	-	0.04
Max	3.7	2.5	0.3	0.1	0.02	0.04	0.02	0.004	0.015	0.02	0.01	0.04	0.06
350 mm^3	3.57 ± 0.03	2.36 ± 0.12	0.17 ± 0.05	0.07 ± 0.04	0.01 ± 0.01	0.03 ± 0.01	0.00	0.00	0.01 ± 0.005	0.01 ± 0.01	0.005 ± 0.005	0.034 ± 0.005	0.05 ± 0.01
700 mm^3	3.60 ± 0.05	2.31 ± 0.10	0.18 ± 0.04	0.08 ± 0.04	0.01 ± 0.01	0.03 ± 0.01	0.00	0.00	0.01 ± 0.005	0.01 ± 0.01	0.005 ± 0.005	0.035 ± 0.007	0.05 ± 0.01
1000 mm^3	3.59 ± 0.04	2.31 ± 0.10	0.18 ± 0.06	0.07 ± 0.05	0.02 ± 0.01	0.02 ± 0.01	0.00	0.00	0.01 ± 0.005	0.01 ± 0.01	0.005 ± 0.005	0.035 ± 0.008	0.05 ± 0.01

For the mold, silica sand was used in sufficient quantity to cover the casting. Metal brackets held the sand mold shape during casting, and coolers and feeders were avoided. The removal of the brackets occurred when a surface temperature of 400 °C was reached, according to the cooling simulations (Table 4).

Table 4 Times required for each analyzed cube to reach surface temperatures defined by simulation data

Cube	400 °C	300 °C
350 mm × 350 mm × 350 mm	34 h	42 h
700 mm × 700 mm × 700 mm	109 h	131 h
1000 mm × 1000 mm × 1000 mm	170 h	200 h

2.2 Microstructural and mechanical characterization

Fifteen samples for each condition (three samples for each of the five foundries) were extracted by saw cutting; attention was paid to avoid thermal alteration of the microstructure. Microstructural analyses were carried out on the samples using optical microscopy (OM) and field emission-gun scanning electron (FEG-SEM) microscopy, equipped with energy-dispersive X-ray spectroscopy (EDS). Metallographic samples were embedded in conductive resin, ground by emery papers from 180 grit up to 1200 grit, and polished by diamond suspensions from 9 to 1 µm, according to the ASTM E3 standard. Finally, metallographic samples were etched with 4% Nital reagent (4 mL HNO_3-96 mL ethyl alcohol) according to the ASTM E407 standard. Image analysis was done using ImageJ software to identify nodularity, *N* (%), nodule count, *NC* (units/mm^2), nodule size, *NS* (mm^2), ferritic grain size, *FG* (intercepts/mm), and pearlitic area, *PA* (%). Analysis areas for graphite characterization were carried out considering the size of the graphite nodules due to the long solidification times. Three different images were captured per sample, each measuring 3.2 mm × 5.7 mm, for a total analysis area per sample of approximately 55 mm^2. For the graphite analysis, the ISO 945-4:2019 standard was applied as far as possible, considering no

references for sections larger than 200 mm. In particular, nodularity for each area was evaluated according to Eq. (1):

$$Nod = \frac{A_V + A_{VI}}{A_{all}} \quad (1)$$

where *Nod* is nodularity, in %; A_V and A_{VI} represent the total area of graphite particles with roundness ≥ 0.6 to ≤ 1.0 (only form V and VI particles by ISO 945-4:2019 are included as spheroidal graphite particles in the nodularity calculation); and A_{all} is the total area of all graphite particles that meet the size criteria, excluding the particles that intersect the border of the area of analysis. Roundness is a shape factor calculated as the area of a graphite particle divided by the area of the circle where the diameter is the maximum Féret diameter of the same graphite particle.

Nodules along the edges and nodules characterized by a Féret diameter less than 30 µm (class 6 and lower according to the ISO 945-4:2019 standard) were excluded from the calculation of nodularity and average nodule size. Based on the magnification applied for quantitative analysis, this threshold was set to eliminate measurement errors introduced by scratches, noise, and small pores. Only the particles with a minimum roundness equal to 0.6 (according to the ISO 945-4:2019 standard) were analyzed for nodule count. Furthermore, areas with degenerated graphite were manually counted as degenerate and excluded from the images to facilitate automated analysis of the nodules.

According to the ASTM E112-13 (2021) standard, the intercept method was used to measure the ferritic grain dimension. The pearlitic area was evaluated using the percentage of occupied area within the analysis area.

Brinell hardness (HB30) was carried out according to the ASTM E10-18 standard with a 2.5-mm steel ball, 187.5 kg load, and dwell time of 10 s to assess the correlation between solidification time and mechanical properties. Hardness was evaluated on each specimen and calculated as the average of at least three measurements for each sample.

3 Results and discussion

Significant microstructural differences were observed between the different solidification conditions (solidification time: 3, 10 and 20 h, and casting position: casting center (C), and transition zone (T)) on the microstructural characteristics of the EN-GJS-400-15, as summarized in Table 5 and Fig. 2 and highlighted by representative microstructures shown in Figs. 3 and 4.

Table 5 Results of image analysis measurements carried out on specimens characterized by different solidification conditions: *N* (%), *NC* (units/mm^2), *NS* (mm^2), *PA* (%) and *FG* (intercepts/mm)

	3C			10C			10T			20C		
	Min	Max	Average	Min	Max	Average	Min	Max	Average	Min	Max	A
	88.9	95.6	91.4 ± 2.3	57.1	90.7	82.4 ± 11.6	50.2	95.8	83.2 ± 14.0	43.3	91.1	7 17.

units	22.6	41.0	30.3 ± 7.1	5.3	19.0	10.3 ± 4.3	1.7	12.2	4.5 ± 2.8	2.0	6.3	3 1.1
mm^2	0.002	0.005	0.004 ± 0.001	0.006	0.017	0.012 ± 0.003	0.010	0.039	0.026 ± 0.009	0.019	0.036	0 0.0
%	0.0	7.9	3.7 ± 2.8	3.3	18.3	8.4 ± 3.9	0.0	13.8	5.3 ± 4.1	1.5	25.2	1 7.2
intercepts	19.1	23.1	20.5 ± 1.4	11.4	19.5	15.4 ± 2.0	10.5	15.7	12.9 ± 1.4	7.9	13.6	1 1.6

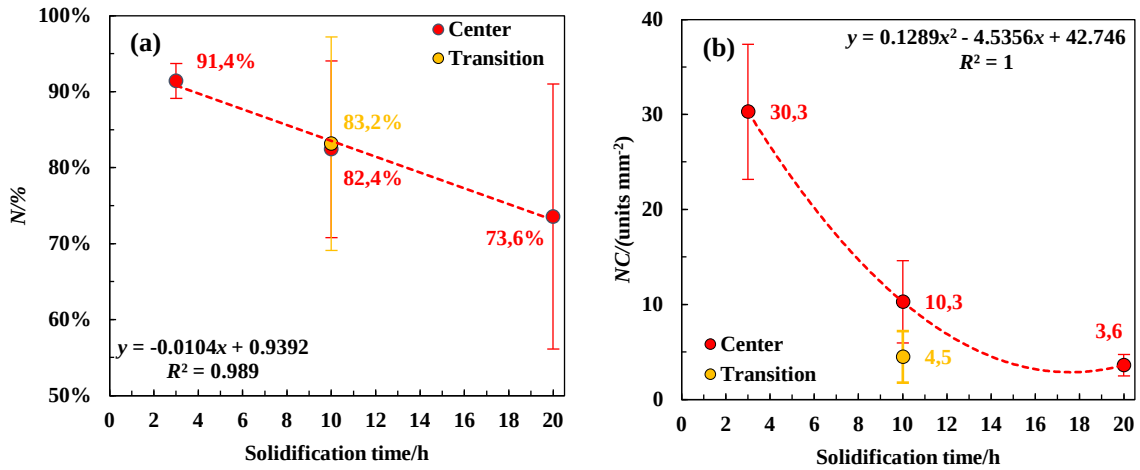

245

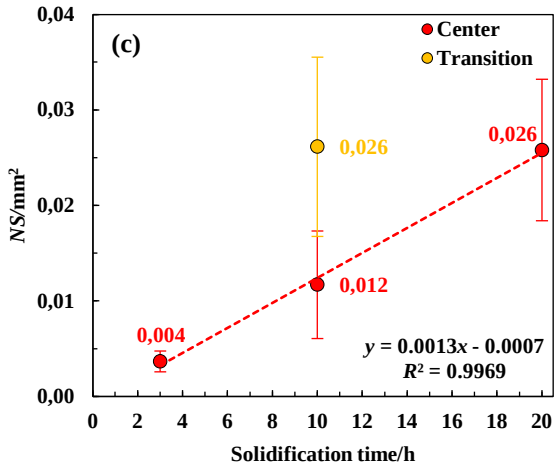

246

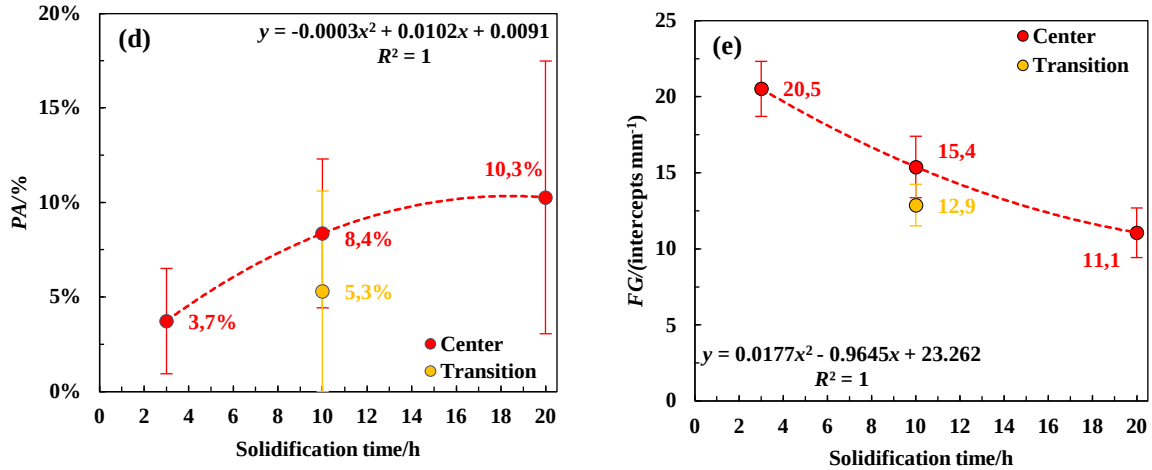

247

248 Fig. 2 Effects of different solidification times (3, 10 and 20 h) and casting positions (casting center and transition
249 zone) on microstructural characteristics of EN-GJS-400-15. **a** Nodularity; **b** nodule count; **c** nodule size; **d** pearlitic
250 area extent; **e** ferritic grain size. R^2, referred to as the square of the correlation, measures the proportion of variation
251 in the dependent variable that can be attributed to the independent variable.

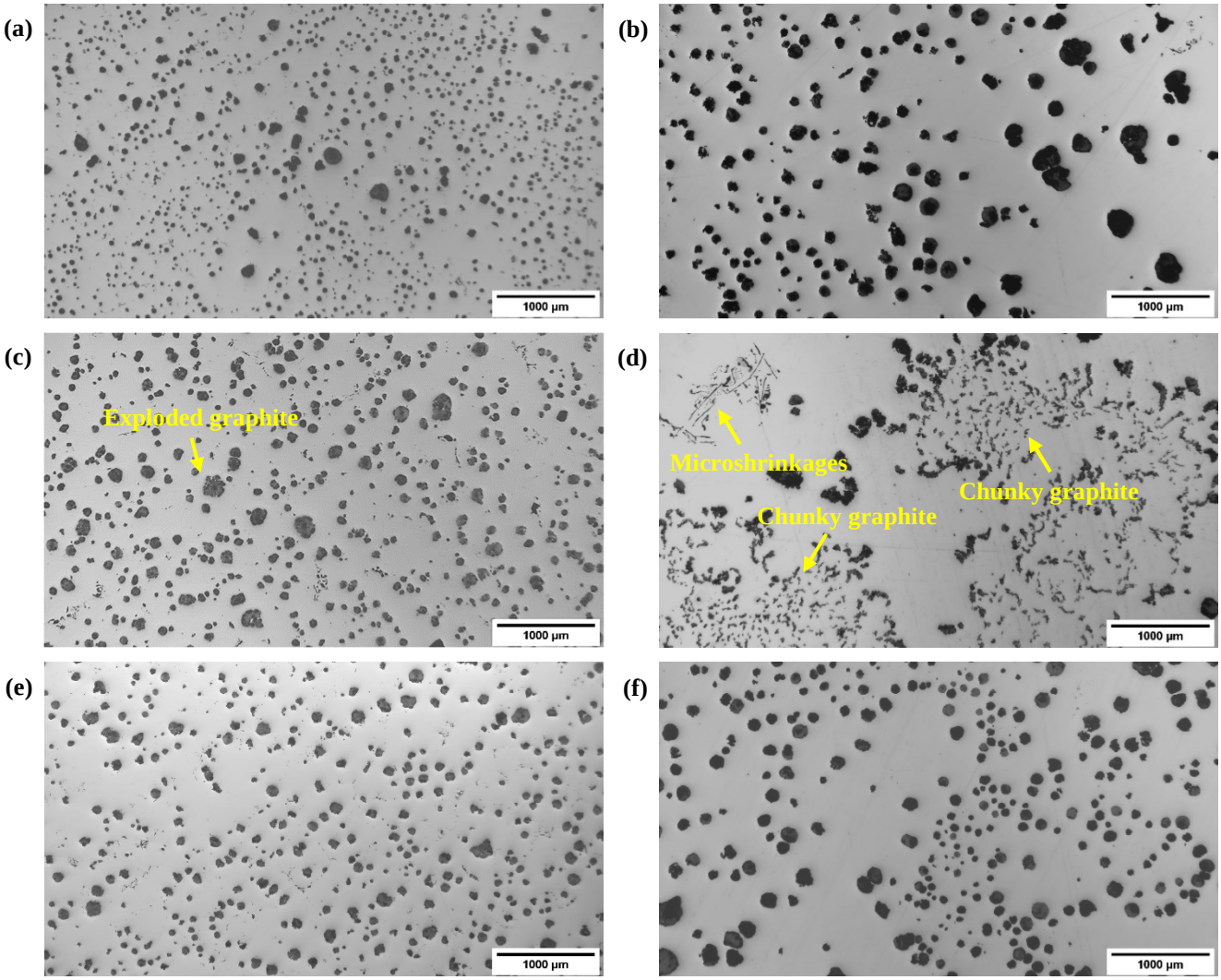

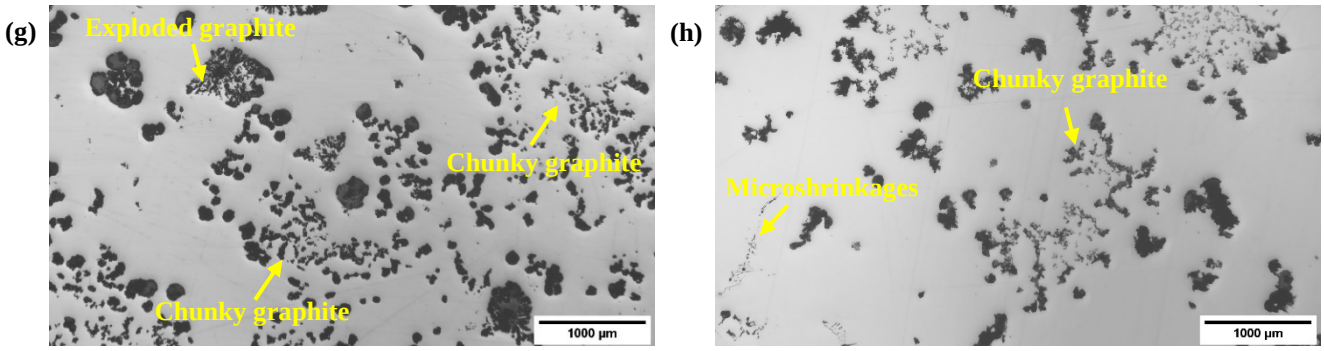

252 Fig. 3 EN-GJS-400-15 microstructures from solidified samples under different solidification conditions. **a, c** 3C
253 condition; **b, d** 20C condition; **e, g** 10C condition; **f, h** 10T condition. The first image of each solidification condition
254 shows the best identified microstructural features, the second one the worst.

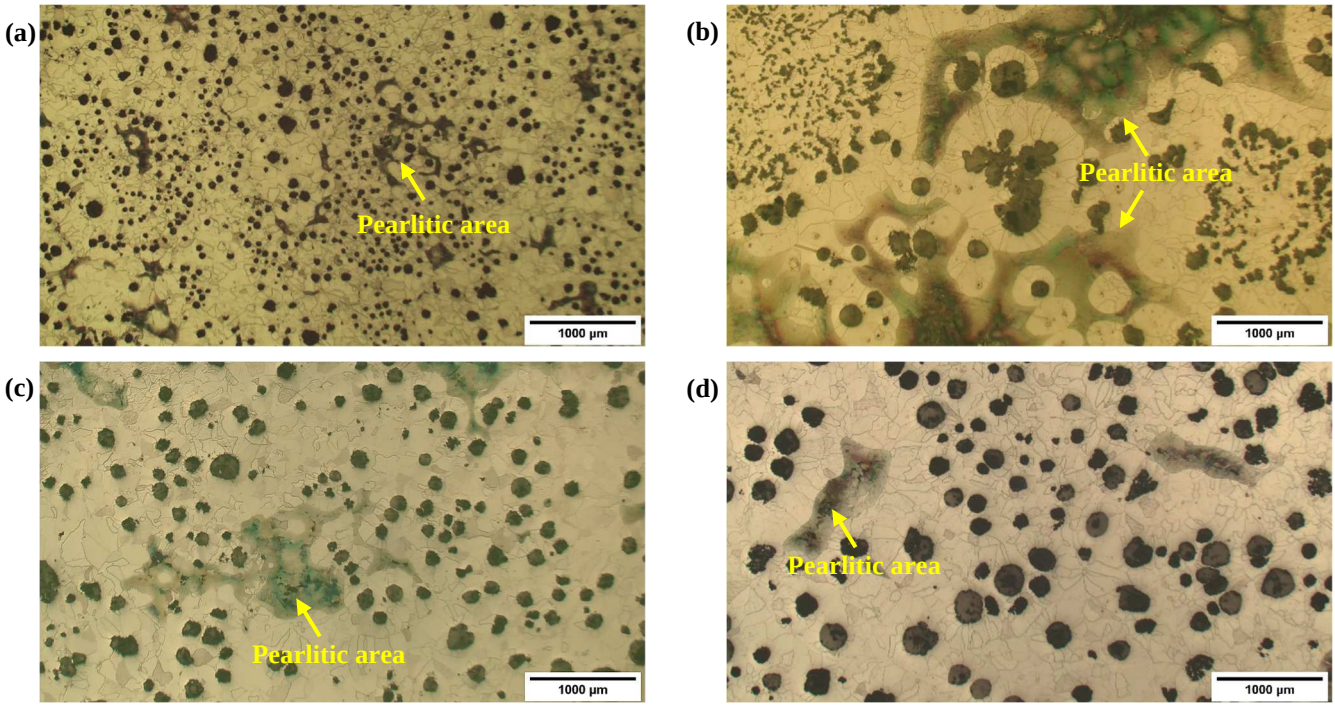

255 Fig. 4 EN-GJS-400-15 microstructures from solidified samples under different solidification conditions. **a** 3C
256 condition; **b** 20C condition; **c** 10C condition; **d** 10T condition

257 As shown in Fig. 2, the microstructural characteristics of the casting center (in terms of graphite nodules and
258 ferrous matrix) strongly depend on the increase in solidification times, as also described in the literature for thinner
259 wall thicknesses [10, 24–26].

260 Focusing on the casting center position (C condition), the increase in the solidification time (from 3 to 20 h) leads
261 to a decrease in *NC* (from 30.3 to 3.6 nodules per mm^2) and an increase in *NS* (from 0.004 to 0.026 mm^2) (Fig. 2a,
262 c). At the same time, as solidification time increases, the morphology of the nodules "degenerates" as a result of the
263 formation of exploded and chunky graphite (Fig. 3d, h), with a decrease in *N* from 91.4% of the 3C condition to
264 73.6% of the 20C condition (Fig. 2b). Longer solidification and cooling times (Table 4) also lead to an increase in

inhomogeneity in terms of morphology and size of the graphite nodules, with very marked differences between different samples under the same solidification conditions (time and position) (Table 5 and Fig. 2). This result is also due to the production of castings by different foundries, which amplified the microstructural variability of the samples under the same solidification conditions due to the complexity of the nucleation and segregation phenomena. Large nodules are associated with primary graphite growth due to solid solution diffusion mechanisms below the eutectic temperature [22]; prolonged exposure to high temperatures due to extremely long cooling times (Table 4) leads to continued growth of primary nodules. However, the asymptotic value of *NC* equal to 3.6 nodules per mm^2 may indicate a limit in the increase in nodule size imposed by the solid solution diffusion of C atoms and the consequent achievement of the maximum mean nearest neighbor distance between nodules, as well as to a limit in obtaining nodules without generating degenerate graphite.

The degenerate graphite, observable for 10 and 20 h of solidification time (Fig. 3d, g, h), results from the combined effect of limited undercooling and increased liquid supersaturation, negatively influencing the nodule growth mechanisms. As described by Källbom et al. [25], the solid solubility of rare earth (RE), Mg, S, and O in austenite is negligible; therefore, these elements gradually enrich the liquid at the solidification front, thus influencing the growth of the eutectic graphite. On the one hand, the nodulizing effect of Mg and RE makes the growth of eutectic graphite possible along the crystalline orientation <0 0 0 1>, spheroidizing the graphite particles; on the other hand, S, O, and excessive Mg and RE content promote the branching of eutectic graphite, which assumes the chunky or exploded morphology (Fig. 3d, g, h). This condition was favored in the center of the casting, where the advancement of the solidification front led to a continuous enrichment of the liquid melt in Mg or RE and the subsequent degeneration of the graphite nodules. An example is the presence of distinct endogenous inclusions such as magnesium oxides (MgO) in the intercellular region (Fig. 5) formed during solidification due to the continuous enrichment of Mg in the residual melt and its reaction with dissolved O. The action of O is doubly damaging: on the one hand, it traps Mg and favors the formation of degenerate graphite; on the other hand, it forms non-metallic MgO compounds that worsen the mechanical properties of the castings. Therefore, it is essential to control the MgO formation during pouring.

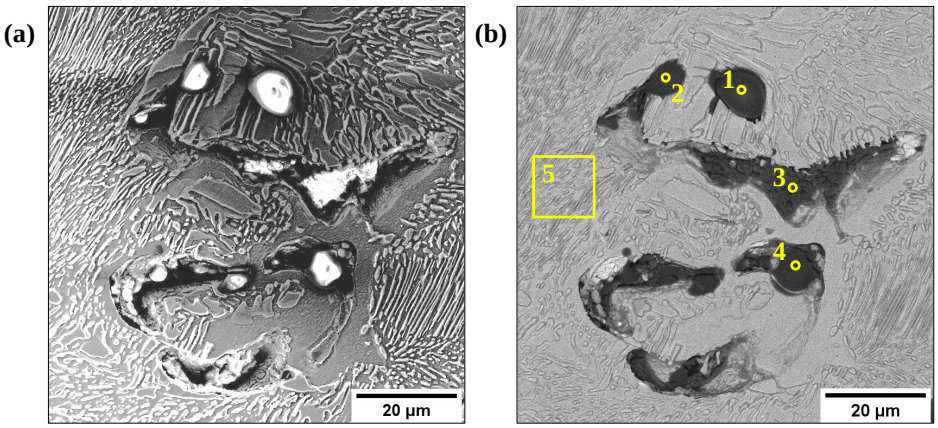

Normalized atomic concentration/%	C	O	Mg	Si	P	S	Fe
1	18.0	57.4	21.0	0.0	1.9	0.0	1.7

2	20.8	59.0	17.7	0.0	2.2	0.1	0.2
3	20.2	56.8	19.7	0.1	1.2	0.2	1.8
4	20.8	58.8	19.1	0.0	0.4	0.0	0.9
5	23.6	1.6	0.0	1.6	0.0	0.0	73.2

Fig. 5 High magnification SE (secondary electrons) (**a**) and BSE (Back-scattered Electrons) (**b**) images of MgO inclusions in intercellular regions of a 20C sample. EDS analysis of panel "5" in (**b**) shows composition of pearlite (ferrite and cementite lamellae, Fe_3C)

For atomically smooth (faceted) interfaces, such as graphite, the spheroidization process requires large driving forces that necessitate high undercooling and supersaturation of the nodulizing elements in the liquid melt [5]. As the wall thickness and solidification times increase, the driving forces become too low to promote spheroidal graphite. However, they are sufficient to form lamellar graphite, as also reported in [21, 27], resulting in a spiral growth mechanism on the "c" axis of graphite crystals capable of forming dendritic (coarse and exploded) graphite, observable in Fig. 3d, g, h as aggregates or clusters of graphite particles. The distribution of the chunky graphite is not uniform, and it is possible to identify fine chunky graphite (Fig. 3d) and coarse chunky graphite (Fig. 3g) depending on the solidification time and extension of the affected areas.

An additional factor that increases the formation of degenerate graphite is the increase in the content of interfering elements in the intercellular zones, which favors the formation of blocky graphite (Al, Ca, Ce, Ni, and Si) or lamellar graphite (As, B, Bi, Cu, Pb, Sb, and Sn) [28, 29]. In particular, as the solidification time increases, the interfering elements have enough time to diffuse onto the boundary surface of the graphite melt, thus interrupting the spheroidization of graphite and promoting another graphite morphology. Comparable mechanisms led to a three-fold increase in the *PA* extension, moving from the 3C to the 20C condition. As solidification times increase, the transformation from austenite to ferrite is promoted by C atom diffusion, thus limiting the formation of pearlitic zones in small and homogeneously distributed intergranular areas in the ferritic matrix (Fig. 4a). However, longer solidification time facilitated segregation phenomena and the accumulation of pearlite promoter elements in the liquid melt, such as Cr and Mn, leading to the formation of large intergranular pearlitic areas within a coarse ferritic matrix, and microshrinkages promoted by the precipitation of carbides (Fig. 6a, b). HSDI castings were also affected by a significant coarsening of the ferritic matrix linearly dependent on the solidification time (Fig. 2e): moving from the 3C to the 20C condition, the increase in *FG* is equal to 45.8%.

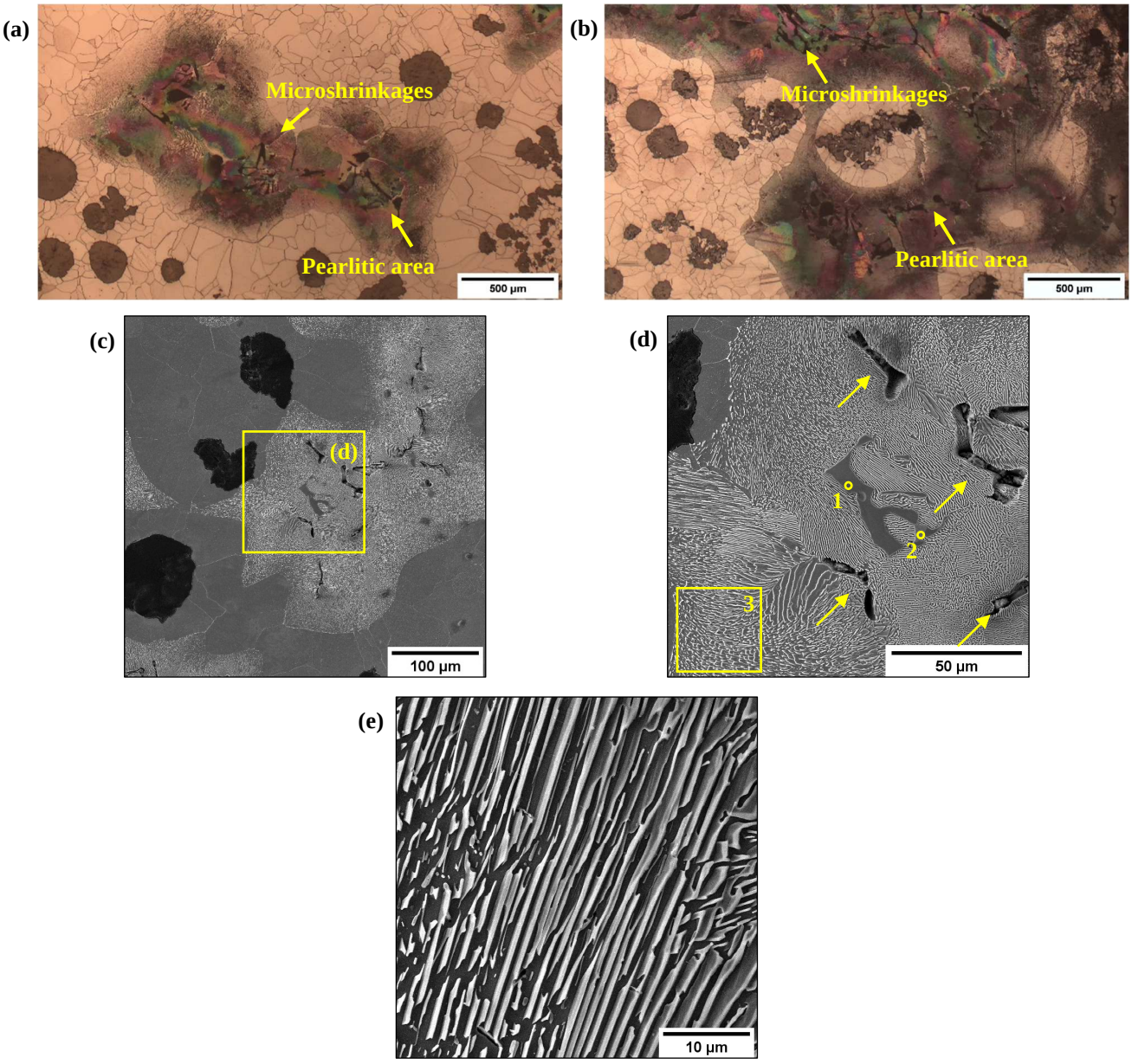

C	Mg	Si	P	S	Ti	V	Mn	Fe	Cr	Cu	Zr	Nb
%												
49.8	0.04	0.00	0.01	0.00	31.6	10.6	0.00	1.6	0.00	0.01	2.51	2.45
50.3	0.04	0.09	0.00	0.00	12.4	3.34	0.03	3.6	0.00	0.12	27.9	1.41
21.4	0.03	1.54	0.00	0.00	0.01	0.24	1.16	74.9	0.52	0.14	0.00	0.00

Fig. 6 Microshrinkages in correspondence with pearlitic area in 10C (**a**) and 20C samples (**b**). High magnification SE images and EDS analysis of intercellular phases segregated in intercellular regions. **c** Pearlitic island; **d** micro shrinkages (yellow arrows) and complex (Ti Zr, and V) carbide (points 1 and 2) embedded into a pearlitic structure; **e** detail of pearlitic lamellar structure. EDS analysis of box "3" in (**d**) shows composition of pearlite (lamellas of ferrite and cementite, Fe_3C)

Hard carbides are present in the intercellular pearlitic regions due to the reduced solubility of carbide-promoting elements in austenite. The area fraction of pearlite and the number of carbides strongly depend on the chemical composition and segregation of pearlite- and carbide-promoting elements in the remaining liquid during eutectic solidification. In particular, Ti, V, Mo, and Nb are present in small amounts in common ferrous charge materials and are typical residual elements in HSDI castings. Although present in very low quantities in the furnace charge, they strongly segregate at the cell boundaries during austenite solidification from the liquid phase, reaching concentrations up to 1000 times higher than those allowed in the nominal concentration (Table 3), thus promoting the formation of Ti-, V-, Mo-, and Nb-based carbides (Fig. 7). In addition, the long solidification times strongly impact nodule density (Table 5 and Fig. 2) and thus the diffusion distance for C and other elements during solidification and cooling in the solid state. This is particularly true under the 10C, 10T, and 20C conditions, where a more pronounced segregation of the promoting elements was favored, increasing the area fraction of carbides formed at the end of solidification. During DI solidification, carbide precipitation can occur directly from the liquid, at the early stage, or at the end of austenite solidification. Considering the long solidification times, the low content of carbide promoters in the chemical composition (Table 3), and the position of the carbides in the microstructure at the intergranular region, embedded into pearlitic regions, the carbide precipitation could mainly occur in the last part of the austenite solidification due to very significant segregation phenomena of carbide promoter elements toward the remaining liquid during eutectic solidification [13]. The analysis highlighted a higher carbide content and microshinkages in the pearlitic areas of the 10C and 20C samples, characterized by a more extensive pearlitic area. Another result that can be observed from Figs. 4b and 6a, b is the proximity of a large number of carbides around the degenerate graphite. As described in [13, 30], the formation of carbides hinders the diffusion of C atoms from austenite to graphite through the ferritic shell, favoring the formation of chunky graphite due to the kinetic disadvantage for the growth of nodules and the thermodynamic conditions for the graphite nucleation at the austenite-liquid interface.

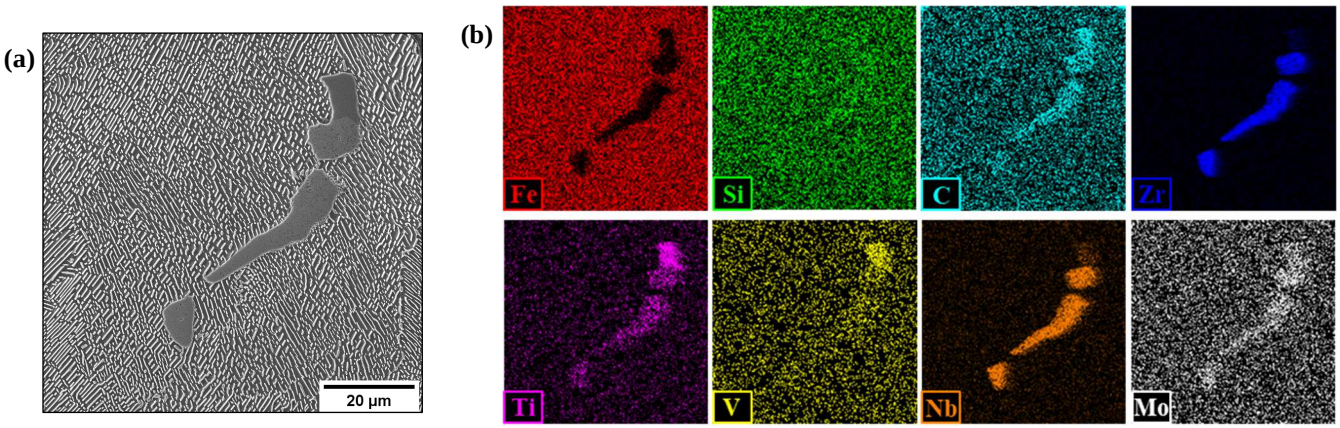

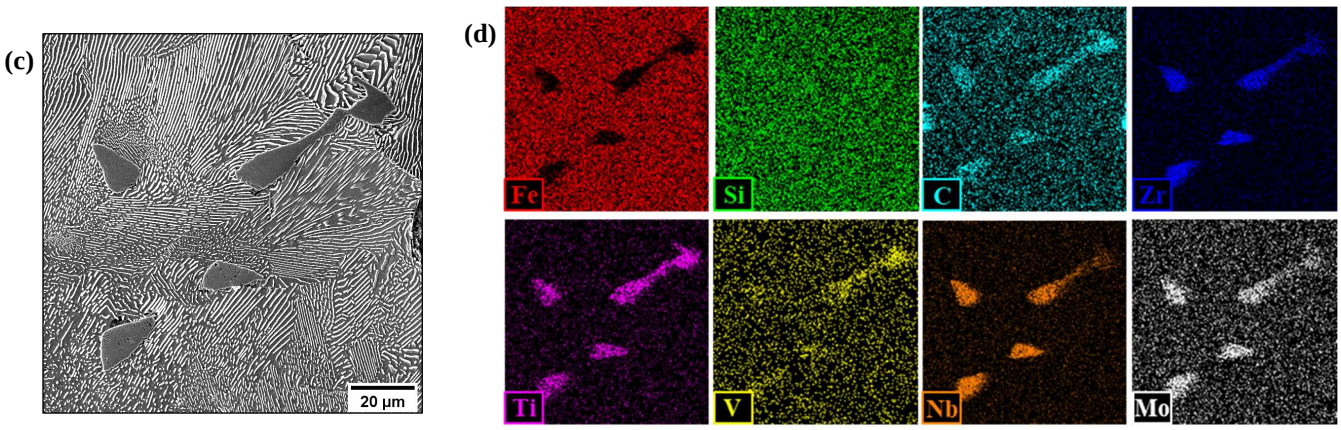

Fig. 7 SE images (**a, c**) and EDS maps (**b, d**) of Ti-, V-, Mo-, Zr-, and Nb-based carbides embedded into a pearlitic structure

In conclusion, segregation phenomena of minor elements at the interface (carbide formers such as Cr, Ti, and V, pearlite promoters such as Mn and Cr, nodularizer and inoculant elements such as Mg, Zr, and RE) induced the formation of large intergranular pearlitic islands in the ferritic matrix (Fig. 6a–e). In addition to "single" carbides, high-entropy carbides are identified in the intercellular regions (Fig. 7); as described by Kan et al. [31], rock-salt crystal structure carbides, such as TiC, ZrC, and NbC, are completely inter-soluble, and, if melted together with Fe, they precipitate out of the melt and form a single high-entropy carbide phase. Carbides are also at least partially responsible for the formation of microshrinkages since they have a smaller volume than the ferritic matrix and graphite after solidification (Figs. 6d and 8). Moreover, very long solidification times, as occurs in the 20C condition, can also lead to the formation of large Fe_3C lamellas in the pearlitic structure, increasing the discontinuity with the ferrous matrix (Fig. 8). As reported in [32] and shown by EDS analysis in Fig. 8, Cr and Mn have a high impact on the formation of the intergranular pearlitic area: they decrease the eutectoid equilibrium temperature at which austenite decomposes into ferrite and graphite, thus leading to a decrease in the carbon diffusion coefficient during the ferritic reaction and favoring the formation of pearlite.

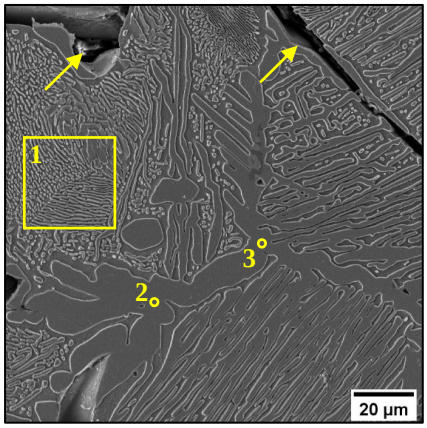

Normalized atomic concentration/%	C	Mg	Si	P	S	Ti	V	Cr	Mn	Fe	Ni	Cu
1	17.7	0.05	1.02	0.00	0.00	0.03	0.14	0.24	1.16	79.50	0.08	0.11
2	26.3	0.02	0.10	0.03	0.03	0.00	0.12	0.62	1.11	71.65	0.03	0.01
3	26.5	0.06	0.05	0.00	0.00	0.00	0.18	0.59	1.19	71.42	0.03	0.00

Fig. 8 Large Fe_3C lamellas within pearlitic structure into 20C microstructure. Yellow arrows indicate microshrinkages within pearlitic area

Significant differences were observed even for the samples characterized by the same solidification time (10 h) but by different extraction positions (casting center (10C) of 700 x 700 x 700 mm^3 cube or transition zone (10T) of 1000 mm × 1000 mm × 1000 mm cube). The 10T condition is characterized by a *NS* approximately double that of the 10C condition and a lower *NC* (–56.3%), while the *N* is comparable (82.4% vs. 83.2%, respectively). At the same time, the *PA* of the 10T condition is smaller than the 10C condition (–36.9%), and the *FG* is coarser, with an increase equal to 16.2% (Fig. 2).

The differences between the 10T and 10C microstructures (Figs. 3 and 4) can be explained by considering three main phenomena which take place during solidification in HSDI castings: (i) graphite nucleation and growth, (ii) ferritic grain formation and coarsening, and (iii) segregation of minor elements.

The formation of a non-homogeneous microstructure in HSDI castings, characterized by large pearlitic islands (Fig. 5), is promoted by segregation of pearlitic promoters such as Mn and Cr in the intercellular regions of the ferritic matrix. Therefore, the formation of large pearlitic islands affects the casting center (10C condition) more than the transition zone (10T condition) due to the segregation of alloying elements into the last fraction of liquid that solidifies (Fig. 2d).

The size and morphology of graphite in as-cast DI result from crystallization within the liquid and growth in the austenitic shell controlled by C atom diffusion. Instead, solid solution diffusion mechanisms below the eutectic temperature increase the *NS* and reduce the *NC* due to C atom diffusion. In particular, dissolution of smaller particles and deposition onto larger particles occurs to reach a more thermodynamically stable state where the surface-to-area ratio is minimized (Ostwald ripening mechanism). Considering the longer time necessary for the largest cube (1000 mm × 1000 mm × 1000 mm) to cool (200 h to reach 300 °C on the surface) compared to the medium cube (700 mm × 700 mm × 700 mm) (131 h to reach 300 °C on the surface) (Table 4), the 10T samples are subjected to high temperature for a longer time than the 10C samples, even if the solidification times are comparable. Therefore, castings with a higher thermal modulus favor the formation of a lower number of larger graphite nodules in the transition zone.

The comparable *N* can be explained based on the peculiar graphite growth conditions in the center of the HSDI castings [20, 21]. Initially, the graphite nuclei precipitate in the liquid, and then spheroids are formed by the action of Mg and RE; however, during the coarsening of the first nuclei, the morphology of the graphite nodule can degenerate. The development of anomalous structures of the graphite (exploded or chunky graphite) is due to high C atom supersaturation in the remaining liquid and low nucleation potential related to the lack of oxygen-based compounds suitable for graphite nucleation [25] or insufficient undercooling [33]. Consequently, the chunky or exploded graphite formation occurs during solidification and depends on the solidification time. In this condition, the casting center is disfavored compared to the transition zone at equal solidification time due to the more extensive segregation phenomena (e.g., Mg, Mn, Mo, Cr, V, B, Ti) around the coarse eutectic cells, which can negatively impact nodularity [12].

Local segregation also occurs in the transition zone of the 1000 mm^3 cube due to the large size of the casting. This leads to the formation and growth of chunky graphite cells by diffusion of C atoms through the austenitic matrix and, consequently, to the growth of very large foliated dendrites and branched structures (Fig. 3h) depending on the cooling time. Therefore, the slow cooling rate after solidification favors the growth of chunky and exploded graphite in the 10T condition more than in the 10C condition. In addition, the longer exposition at high temperature negatively affects *N* (Table 4) and induces the coarsening of the ferrite grains, as reported in Fig. 2e.

Despite the excellent castability of DI, interdendritic shrinkage defects (sized up to a Féret diameter of 300 µm) were observed, especially in samples extracted from the casting center for longer solidification times (10C and 20C conditions), as shown in Fig. 9. As a matter of fact, the Mg segregation in the center of the large castings can favor a more extensive formation of interdendritic shrinkage [34]. At the same time, the solidification of the DI as a divorced eutectic, i.e. the graphite nodules surrounded by the austenite shell, hinders the interdendritic feeding and promotes the formation of interdendritic shrinkage, as described in [35].

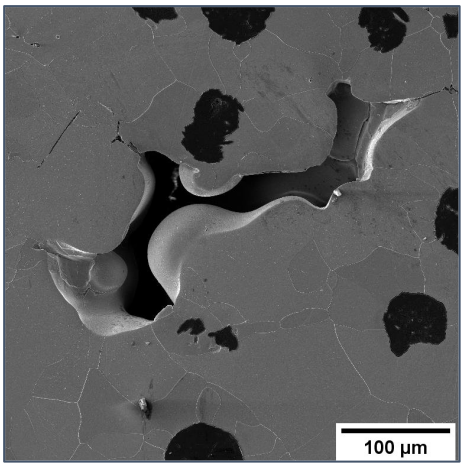

Fig. 9 SE image of intercellular shrinkage within ferritic matrix (10C sample)

As reported in [25, 30, 36], the hardness of DI is essentially the hardness of the ferrous matrix (ferritic and pearlitic grains), increased by the hard carbides located in the intergranular zone. Hardness is minimally influenced by the morphology and size of the graphite, even if the chunky graphite interrupts the continuity of the three-

dimensional matrix. However, optimizing the nodule size and nodule density can indirectly increase the hardness of the DI [37]: a high nodule count allows for obtaining a finer and more homogeneous matrix, thus reducing the presence of defects. In addition, the nodule count is related to the nodularity: if the inoculation treatment is performed correctly, it allows for the obtaining of smaller and more spherical nodules, refining the grain structure.

Despite the significant differences in the microstructures observed in this study, the hardness varies only by 6.6% (Fig. 10) from the maximum value (3C condition: 140.8 HB30) to the minimum value (20C condition: 131.5 HB30). This result is due to the combined and contrasting effects related to the variation of the microstructural characteristics described in Fig. 2. This is also supported by the increased data deviation from the 3C to the 20C condition (Fig. 10), which agrees with the microstructural inhomogeneity increase in Fig. 2.

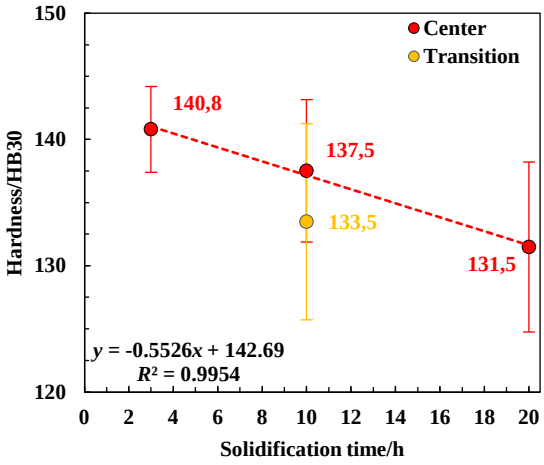

Fig. 10 Effects of different solidification times (3, 10 and 20 h) and extraction zones (casting center, C, and transition zone, T) on hardness of EN-GJS-400-15. R^2 is evaluated only for C samples (different solidification times at casting center)

In HSDI castings, the inoculation and spheroidization treatments are challenging due to the casting size and solidification time. As a result, it is more likely to find areas with low nodule count and segregation of elements that favor the formation of pearlite, carbides, or degenerate graphite. These microstructural irregularities significantly impact the tensile and fatigue properties of the castings [3, 4, 9–11, 24]. However, because hardness is negligibly affected by such inhomogeneities and anomalies, it is not a reliable indicator of the microstructure in HSDI castings and, moreover, it doesn't provide reliable information on tensile and fatigue strength.

4 Conclusions

1. As the solidification time in the center of HSDI varies from 3 to 20 h, the nodule count decreases from 30.3 to 3.6 nodules per $mm^{2,}$ and the nodule size increases from 0.004 to 0.026 mm^2. At the same time, nodularity reduces from 91.4% to 73.6%. These effects are attributed to an increase in local segregation and lower undercooling.

2. For comparable solidification time (10 h), the microstructural characteristics vary in relation to the extraction zone. Specifically, the transition zone (10T) is characterized by an average nodule size approximately double that of the casting center (10C) (0.012 vs. 0.026 mm^2), as well as lower nodule count values (4.5 vs 10.3 nodules per mm^2). Conversely, nodularity is comparable (83.2% vs. 82.4%, respectively).

3. Long solidification times favor the formation of chunky graphite, especially in the casting center, where solidification conditions limit undercooling and promote supersaturation of minor elements in the molten liquid.

4. With increasing solidification time, local segregation phenomena of minor elements increase, thus leading to the formation of carbides in the intercellular area and a three-fold increase in the pearlitic area extension from the 3C to the 20C condition. Conversely, the 10T condition shows a decrease in the pearlitic area extent compared to the 10C condition (5.3% vs. 8.4%, respectively).

5. The increase in casting wall thickness leads to a ferritic grain coarsening from 3C to 20C condition (from 20.5 to 11.1 intercepts per mm). Similarly, the diffusion mechanisms lead to larger grains in 10C than in 10T condition (15.4 vs. 12.9 number of intercepts per mm, respectively).

6. Hardness is slightly influenced by solidification time and varies from the maximum value of 140.8 HB30 for the 3C condition to the minimum value of 131.5 HB30 for the 20C condition. This can be related only to the microstructural coarsening of the graphite nodules and the ferrous matrix.

In the light of the above, the longer the solidification time, the worse the microstructural characteristics of cast iron due to unfavorable solidification phenomena. However, the evaluation of how much the morphology of the microstructure can worsen in terms of nodule size, degenerated graphite, shrinkage porosity, etc., was never evaluated in real castings despite its importance. Moreover, these data will be helpful in refining casting simulations used to predict microstructure in HSDI castings. This would also allow for the optimization of the design of castings and the reduction of costs and environmental impact. This study pointed out that hardness tests do not highlight the microstructural variabilities within ferritic HSDI castings, which instead profoundly affect the static and cyclic mechanical properties, as reported in the literature. This aspect will be explored more thoroughly in future works by the Authors by analyzing the static and cyclic mechanical properties of the EN-GJS-400-15 in the same solidification conditions. Finally, this study establishes a foundation for developing an international standard for quality control of ferritic HSDI castings with thicknesses exceeding 200 mm, currently outside the existing standard.

Acknowledgments

The authors gratefully acknowledge “Fonderie Mora Gavardo-Cast Iron Division, Technical and Metallurgical R&D Team”, “VDP Fonderia”, “Fonderia Vigevanese”, “Fonderia Bocacci”, “Fonderia Ariotti”, “SACMI Group”, and “Zanardi Fonderie SpA” for the fruitful collaboration within the Italian Cast Iron and Steel Unification Body

(Ente Italiano di Unificazione Siderurgica – UNSIDER). Thanks also to Dr. Giacomo Bertuzzi, Dr. Matteo Cova (SACMI), and Dr. Matteo Veronese (Fonderia Vigevanese) for the fruitful collaboration.

Declarations

The authors declare that they have no known competing financial interests or personal relationships that could have appeared to influence the work reported in this paper. The corresponding author, on behalf of all authors, certify that they have NO affiliations with or involvement in any organization or entity with any financial interest (such as honoraria; educational grants; participation in speakers' bureaus; membership, employment, consultancies, stock ownership, or other equity interest; and expert testimony or patent-licensing arrangements), or non-financial interest (such as personal or professional relationships, affiliations, knowledge or beliefs) in the subject matter or materials discussed in this manuscript.

References

[1] M. Benedetti, V. Fontanari, D. Lusuardi, Eng. Fract. Mech. 206 (2019) 427-441.

[2] A. Morri, L. Ceschini, S. Toschi, S. Masaggia, J. Materi Eng And Perform 28 (2019) 3864-3877.

[3] E. Foglio, M. Gelfi, A. Pola, S. Goffelli, D. Lusuardi, Int. J. Met. 11 (2017) 33-43.

[4] Y.N. Pan, C.C. Lin, R.M. Chang, Int. J. Cast Met. Res. 25 (2012) 301-306.

[5] D.M. Stefanescu, G. Alonso, R. Suarez, Metals 10 (2020) 481.

[6] L. Ceschini, A. Morri, A. Morri, E. Salsi, R. Squatrito, I. Todaro, L. Tomesani, Int. J. Cast Met. Res. 28 (2015) 365-374.

[7] L. Ceschini, A. Morri, A. Morri, J. Materi Eng And Perform 26 (2017) 2583-2592.

[8] L.M. Åberg, Trans. Indian Inst. Met. 68 (2015) 1007-1011.

[9] T. Borsato, P. Ferro, F. Berto, C. Carollo, Eng. Fail. Anal. 79 (2017) 902-912.

[10] T. Borsato, P. Ferro, A. Fabrizi, F. Berto, C. Carollo, Int. J. Fatigue 145 (2021) 106137.

[11] M. Benedetti, E. Torresani, V. Fontanari, D. Lusuardi, Metals 7 (2017) 88.

[12] J. Lacaze, Int. J. Met. 11 (2017) 44-51.

[13] M. Riebisch, B. Pustal, A. Bührig-Polaczek, Int. J. Met. 14 (2020) 1152-1161.

[14] Voigt, R. Trace (minor) elements in cast irons. In ASM handbook Vol. 1A Cast Iron Science and Technology; Stefanescu, D.M., Ed.; ASM International: Materials Park, OH, USA, 2017, pp 177–181.

[15] Y. Feng, M. Ma, C. Wang, L. Wang, W. Jiang, E. Guo, Trans. Indian Inst. Met. 76 (2023) 2669-2679.

[16] S. Yamamoto, Y. Fujikawa, H. Itofuji, M. Hatate, S. Hiratsuka, Int. J. Met. 18 (2024) 1994-2002.

[17] J. Sertucha, G. Artola, U. de la Torre, J. Lacaze, Materials 13 (2020) 5402.

[18] L. Tong, Q. Zou, J. Jie, T. Li, Z. Wang, Int. J. Mater. Res. 111 (2020) 385-391.

[19] R.B. Gundlach, J.M. Tartaglia, Int. J. Met. 18 (2024) 1883-1908.

[20] D.M. Stefanescu, G. Alonso, P. Larrañaga, E. De la Fuente, R. Suarez, Acta Mater. 139 (2017) 109-121.

[21] W. Baer, Int. J. Met. 14 (2020) 454-488.

[22] R. Gerghu, L. Magnusson Åberg, J. Lacaze, Mater. Sci. Forum 790-791 (2014) 435-440.

[23] T. Borsato, P. Ferro, F. Berto, Fatigue Fract. Eng. Mater. Struct. 41 (2018) 1746-1757.

[24] T. Borsato, P. Ferro, F. Berto, C. Carollo, Metals 9 (2019) 24.

[25] R. Källbom, K. Hamberg, M. Wessén, L.E. Björkegren, Mater. Sci. Eng. A 413 (2005) 346-351.

[26] D.M. Stefanescu, G. Alonso, P. Larrañaga, R. Suarez, Acta Mater. 103 (2016) 103-114.

[27] J. Lacaze, L.M. Åberg, J. Sertucha, Keith Millis, World Symposium on Ductile Cast Iron: 15–17 October, Nashville. Red Hook (NY): Curran, 360–368.

[28] F. Stieler, D. Funk, B. Tonn, Int. J. Met. 17 (2023) 1315-1325.

[29] J. Lacaze, I. Asenjo, S. Méndez, J. Sertucha, P. Larrañaga, R. Suárez, Int. J. Met. 6 (2012) 35-42.

[30] C. Liu, Y. Du, X. Zhu, Z. Wang, X. Wang, C. Yang, C. You, B. Jiang, J. Alloys Compd. 1006 (2024) 176361.

[31] W.H. Kan, Y. Zhang, X. Tang, T. Lucey, G. Proust, Y. Gan, J. Cairney, Materialia 9 (2020) 100540.

[32] J. Lacaze, J. Sertucha, L.M. Åberg, ISIJ Int. 56 (2016) 1606-1615.

[33] B. Tonn, J. Lacaze, S. Duwe, Mater. Sci. Forum 925 (2018) 62-69.

[34] D. Stefanescu, Mechanical properties of ductile irons, in ASM Handbook, Volume 1A, Cast Iron Science and Technology, ASM International: Materials Park, OH, USA, 2017, pp 456–471.

[35] R. Queirós, B. Domeij, A. Diószegi, Int. J. Met. 18 (2024) 1811-1830.

[36] G.M. Goodrich, Ductile iron castings. In ASM Handbook, Volume 15 Casting, Viswanathan, D. Apelian, R.J. Donahue, B. DasGupta, M. Gywn, J.L. Jorstad, R.W. Monroe, M. Sahoo, T.E. Prucha, D. Twarog, Eds.; ASM International: Materials Park, OH, USA, 2008, pp. 856–871.

[37] E. Guzel, C. Yuksel, Y. Bayrak, O. Sen, A. Ekerim, Mater. Test. 56 (2014) 285-288.